Journal of Renewable Materials
DOI:10.32604/jrm.2020.08650
Article

Tech Science Press

Self-Supported Nanoporous Gold with Gradient Tin Oxide for Sustainable and Efficient Hydrogen Evolution in Neutral Media

Xianglong Lu[1], Tianshui Yu[1], Hailing Wang[1], Ruichun Luo[2], Pan Liu[2], Songliu Yuan[1] and Lihua Qian[1,*]

[1]School of Physics, Huazhong University of Science and Technology, Wuhan, 430074, China
[2]School of Materials Science and Engineering, Shanghai Jiao Tong University, Shanghai, 200030, China
*Corresponding Author: Lihua Qian. Email: lhqian@hust.edu.cn
Received: 19 September 2019; Accepted: 14 October 2019

Abstract: Hydrogen evolution reaction (HER) in neutral medium suffers from slow kinetics as compared to that in alkaline or acidic conditions, owing to larger Ohmic loss and low proton concentration. Here we report that a self-supported nanoporous Au-SnO_x (NP Au-SnO_x) catalyst with gradient tin oxide surface could significantly enhance HER activity in neutral buffer solution (0.2 M PBS). The NP Au-SnO_x catalyst exhibits a low onset overpotential of 38 mV and a small Tafel slope of 79 mV dec^{-1}. The current density of 10 mA cm^{-2} is manifested at an overpotential as low as 148 mV, representing the comparable performance of Pt/C catalyst. This high catalytic activity can retain at least 10 hours without any detectable decay. The superior HER activity is proposed to originate from the gradient SnO_x structure and metal/oxide interfaces in nanoporous ligaments. Furthermore, the X-ray photoelectron spectroscopy reveals that the gradient oxide in the ligament is remarkably stable during long-term reaction.

Keywords: Nanoporous metals; electrocatalysts; hydrogen evolution reaction; neutral electrolyte; gradient oxide structure

1 Introduction

Hydrogen is an attractive and promising energy carrier toward the sustainable energy economy owing to its high energy density and environment-friendly production [1-2]. In many approaches to hydrogen production, the electrocatalytic hydrogen evolution reaction (HER) from water splitting is the most economical and effective route for the future hydrogen demands [3-5]. Owing to the appropriate hydrogen binding energy (HBE) that is located near the peak of a volcano plot (Exchange current density *vs.* HBE), Pt and its alloys are currently the most active HER catalysts and play a benchmark for HER electrocatalysts [6-9].

From the electrolyte perspective, many previous studies about the electrochemical HER have been conducted under acidic or alkaline conditions [10-13]. However, the strong acidic and alkaline electrolytes not only require a rigid tolerance of the container during water splitting, but also lead to a deteriorated stability of the electrocatalysts. One possible route to address these issues is to split water in the neutral electrolyte which is more environmentally benign [14]. Moreover, for most water resource on the earth including seawater and river water, the pH is close to neutral in the natural state. So it is of

significance to develop HER catalysts in neutral media, which can power up the devices sailing in the water. However, HER proceeding in a neutral electrolyte sustains slower kinetics in comparison with that in acidic or alkaline media because of the low proton concentration and larger Ohmic loss [15]. To enhance reaction rates at neutral pH, water molecule must act as the reactants. As a result, much higher overpotential should be applied to reach the same level of the electric current density in neutral solution [16-17]. It was reported that several catalysts, including amorphous MoS_x films [18], FeP nanoparticles [19-20], CoP composites [21-22] and CoS film [23] are active for the HER in neutral solutions. Most of these HER catalysts are in form of powders or colloids with low-dimensional or porous nanostructures and immobilized on current collectors by making use of a polymer binder (nafion or PTFE) [24-26]. Such complicated sample preparation process is a time- and cost-consuming process and makes them neither cost-effective nor efficient for practical application.

So far, it is still extremely challenging to improve HER catalytic activity and stability in neutral media [27-28]. The current density is far below than that in acidic or alkaline electrolyte, requiring a high overpotential (>200 mV) to attain the standard current density of 10 mA cm^{-2}. For instance, the HER current density recorded at −0.2 V *vs.* reversible hydrogen electrode (*vs.* RHE) for amorphous molybdenum sulfide on dealloyed nanoporous gold (NPG) is −5.7 mA/cm^2 in 0.5 M H_2SO_4. However, its current density is only 0.48 mA/cm^2 at the same overpotential in 0.2 M phosphate buffer solution (PBS, pH = 7) [29]. In fact, constructing metal/oxide interface is a promising and effective route to enhance HER performance for heterostructured catalysts, such as core-shell structure [30-33]. It was reported that strong interactions between the adsorbed H_2O species and metal oxide surfaces may grant metal/oxide interfaces the ability to promote the water dissociation step in HER by optimizing hydrogen adsorption energy and facilitating the water species adsorption [1, 34]. However, the metal oxides always suffer from the poor conductivity which suppresses charge transport and thereby efficiency of electrocatalysis [35-36]. Inspired by the molybdenum sulfide coated on the NPG [29, 37], the strategy of designing metal oxide on nanoporous ligament can not only make use of highly conductive metallic skeleton and high mass transport efficiency in nanoporous structure, but also enhance the catalytic performance of metal oxide.

Herein, we report a facile and effective method to fabricate a self-supported nanoporous Au-SnO_x (NP Au-SnO_x) composite with gradient oxide on nanoporous Au skeleton surface for efficient hydrogen evolution by means of one-step chemical dealloying. The unique hybrid structureis able to produce hydrogen with high activity and remarkable stability in neutral media.

2 Materials and Experimental

2.1 Fabrications of the NP Au-SnO_x and NPG

$Ag_{65}Au_{33}Sn_2$ and $Ag_{65}Au_{35}$ precursors were prepared by arc melting pure Ag, Au and Sn with a desired atomic ratio under argon atmosphere. After the verification of composition by energy dispersive X-ray spectroscopy (EDX), the alloy ingot was rolled at room temperature to get a ribbon with a thickness of ~25 m. The NPAu-SnO_x was fabricated by corroding $Ag_{65}Au_{33}Sn_2$ alloy ribbon in 69% HNO_3 solution at room temperature for 8 hours. Nanoporous gold (NPG) was also prepared by corroding $Ag_{65}Au_{35}$ in the same condition for comparison. For further removing Sn, the SnO_x-free nanoporous Au catalyst was dealloyed for a second time in a 6 M HCl solution for 12 hours. Those resulting catalysts were carefully rinsed with deionized water for several times to clean up the residual chemicals and used as work electrodes for electrochemical evaluations directly. The Pt/C ink was prepared by mixing 5 mg commercial Pt/C powder (20 wt%, Hesen, HPT020) into 40 μL Nafion (0.05%, Sigma Aldrich) solution containing isopropanol (30%) and water (70%). After a rigorous sonication of 30 min in ice water, 10 μL of the suspension was drop-cast onto a 3-mm-diameter glassy carbon electrode (loading mass: 0.283 mg cm^{-2}) and was dried in air to form a uniform thin film for electrochemical characterizations.

2.2 Microstructural Characterizations

X-ray diffraction (XRD) measurements were carried out ona Rigaku DMAX/2400 X-ray diffractometer with Cu K_α radiation. Scanning electron microscope (SEM) observations were performed with a field-emission scanning electron microscope (JSM-7600F). A JEOL JEM-2100F transmission electron microscope (TEM) with an acceleration voltage of 200 kV was employed to characterize the structure of nanoporous catalysts. The surface atomic structure of the NP Au-SnO_x and NPG were characterized by using spherical-aberration-corrected TEM in a scanning TEM (STEM) mode. X-ray photoelectron spectra (XPS) were obtained in AXIS-ULTRA DLD-600W XPS system with an Al K_α(mono) anode.

2.3 Electrochemical Measurements and Product Analysis

All electrochemical measurements were performed on a CHI 760E electrochemical workstation with a three-electrode cell. A graphite rod was used as counter electrode. All potentials were measured *vs.* a saturated calomel (Hg/Hg_2Cl_2, SCE) reference electrode (saturated KCl, TJ Aida R0232) and converted to RHE reference scale using E (*vs.* RHE) = E (*vs.* SCE) + 0.0591 × pH + 0.244 V. The NP Au-SnO_x and NPG electrodes after dealloying were used as directly as working electrodes for electrochemical measurements. While for the commercially available Pt/C catalysts, its ink with a concentration of 2 mg mL^{-1} was loaded onto glassy carbon electrode. The HER activities were evaluated by linear sweep voltammetry (LSV) at a scan rate of 5 mV/s in aqueous electrolytes of 0.2 M PBS, 0.5 M H_2SO_4 and 0.1 M KOH. The electrolytes were purged with high pure N_2 for 30 min prior to measurements. All electrochemical tests were carried out at room temperature.

Electrolysis for product analysis was performed in a gas-tight electrochemical cell with two compartments separated by a piece of anion exchange membrane (Nafion 212, DuPont). Cathodic compartment cell with working electrode was connected with the gas-sampling loop of a gas chromatograph (GC-9790II, FULI analyzing incorporations) for the continuous cycling. Gas-phase product was automatically sampled every 15 min for quantitative analysis. Argon (Xiangyun Gas Incorporations, 99.999%) was used as carrier gas during the measurement. The GC columns led directly to a thermal conductivity detector (TCD) to quantify H_2. Gas concentration was determined by the peak areas calibrated from standard gas with different concentrations. Faradaic efficiency (FE) of H_2 was calculated by equation $FE = 2nF/Q$, n is the number of moles calculated from GC analysis, F refers to Faraday's constant (96485 C mol^{-1}) and Q represents all the charge passed.

3 Results and Discussion

3.1 Surface Structure of Nanoporous Electrocatalysts

Representative SEM images in Fig. 1(a) and d show porous characters of the NP Au-SnO_x and NPG, respectively. All the samples exhibit bicontinuous skeletons and the interconnected channels. Statistical distributions of nanopores/ligaments are estimated for the NPAu-SnO_x (15.4 nm) and NPG (16.2 nm) (Fig. S1, Appendix A). Relatively smaller pore size in the NPAu-SnO_x results from the sluggish diffusion of Au atoms, which is perturbed by spontaneous releasing and burying of tin atoms into the ligament throughout chemical dealloying [38-39]. The ligaments/pores size can be tuned by the dealloying time and temperatures [40-41]. The concentration of tin element is estimated as 7.3 wt.% based on EDX analysis (Fig. S2, Appendix A). The XRD pattern of the NP Au-SnO_x in Fig. S3 identifies all the crystal planes corresponding to face-centered-cubic (fcc) Au. After close inspection of Au (111) diffraction peak, a small shoulder at the 2θ angle of 37.8° corresponds to the (200) reflection of SnO_2. The XRD result indicates the formation of tin oxide in the ligaments during the dealloying in HNO_3. Spontaneous formation of tin oxide results from the oxidization of tin atoms in nitric acid during the dealloying, and the detailed characterization will be described in the following section. The way of introducing metal/

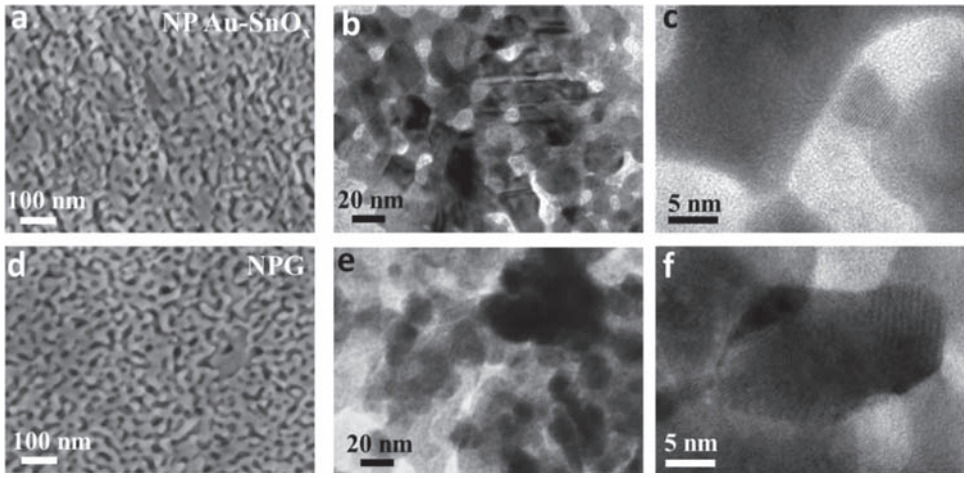

Figure 1: Structures of the NP Au-SnO_x and NPG catalysts. a) SEM and b) TEM images of the NP Au-SnO_x. c) HRTEM image of the NP Au-SnO_x. d)SEM and e) TEM images of the NPG. f) HRTEM image of the NPG

oxide interface in nanoporous structure by adding small fractions of metal into precursor alloy is convenient and cost-effective.

The NP Au-SnO_x catalyst was also examined using STEM characterizations. Fig. 2(a) shows the typical image of the ligament infrastructure for chemical composition evaluation; Fig. 2(b-d) shows the EDX mappings of Au, Sn and O elements, respectively. It is evident that Au and Sn atoms are homogeneously distributed along the ligaments. However, it is also shown that O atoms are enriched at the edge of ligaments in the overlay mapping (Fig. 2(e)). As represented in Fig. 3(a), a dark interface is visible at the ligament edge in high resolution TEM (HRTEM) image, suggesting surface oxide with a thickness of 5~10 nm.

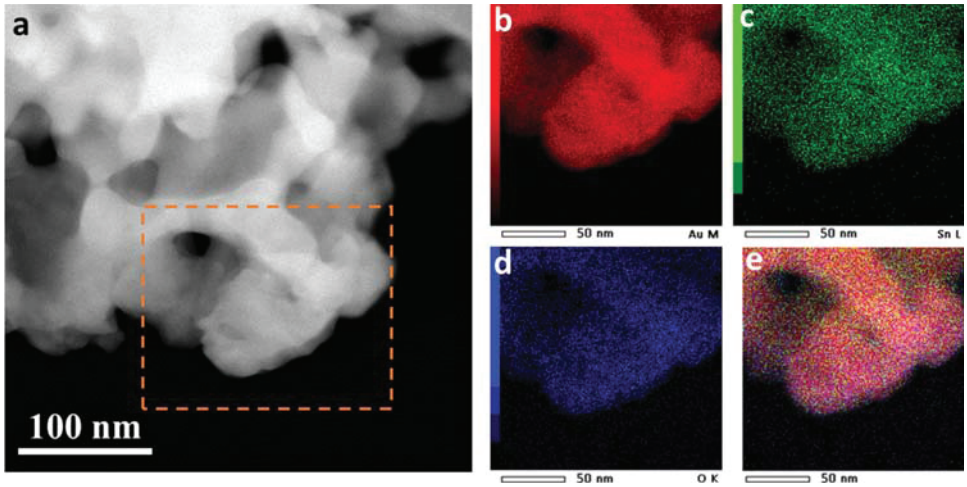

Figure 2: Morphology and chemical composition analyses of the NP Au-SnO_x. (a) Low-magnification STEM bright-field image of the NP Au-SnO_x. The dashed square indicates the region selected for EDX mapping. (b-e) Corresponding elemental mapping images of the NP Au-SnO_x in the selected region showing the spatial distribution of Au (b), Sn (c), O (d) and their overlay (e)

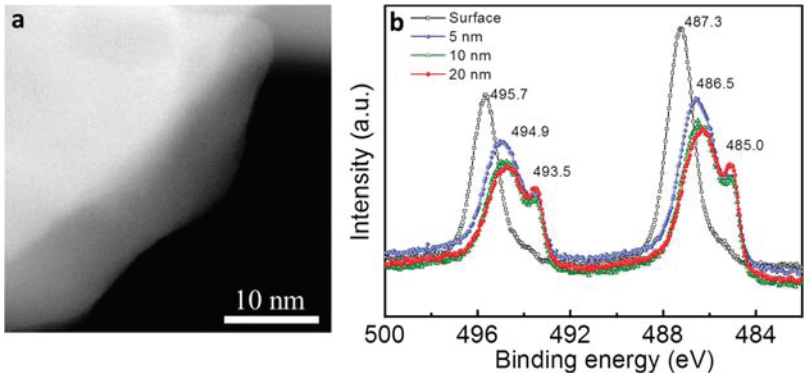

Figure 3: TEM and XPS characterizations of the NP Au-SnO_x. (a) HRTEM image of the NP Au-SnO_x. (b) Sn 3d XPS spectra of the NP Au-SnO_x surface and etched at different thicknesses

More surface analysis requires the XPS characterization, which is capable of providing the detailed information of the oxidation states of tin. In order to reveal the composition evolution with the depth, the ligament can be etched layer by layer by using argon ion beam sputtering (Fig. S4). As shown in Fig. 3(b), a doublet at 495.7 and 487.3 eV is assigned to the $3d_{3/2}$ and $3d_{5/2}$ peaks of Sn (IV) [42]. The percentage of SnO_2 is estimated as 92% by calculating the integral area in the deconvoluted spectrum (Fig. S5). As the etching depth increases, the peak intensities decrease gradually and shift to lower energy. The $3d_{3/2}$ peak at 494.9 and $3d_{5/2}$ peak at 486.5 eV corresponding to Sn (II) can be detected in the depth of 5~20 nm. The paired shoulder peaks at 493.5 and 485.0 eV are related to metallic state (Sn^0) [43]. The atomic concentrations of Au, Sn and O atoms are shown in Fig. S6 based on quantitative analysis. The oxygen concentration decreases from ~20% on the top surface to ~5% in the depth of 5~20 nm, indicating the gradient distribution of tin oxide perpendicular to the ligament surface. The top surface oxide is mainly SnO_2, and the subsurface is dominated by SnO in the internal ligament. This gradient SnO_x structure seems highly stable in the nitric acid. More importantly, homogeneously distributed Sn atoms could create numerous Au/SnO_x interfaces in the ligaments of nanoporous structure. This unique structure with metal/oxide interfaces will enhance catalytic performance significantly, which has been demonstrated in Au/CeO_2, Ni/NiO and Co/Co_3O_4 materials [44-46].

To further reveal the surface composition of the NP Au-SnO_x, cyclic voltammetry (CV) measurements are conducted by sweeping from 0.93 V to −0.07 V *vs.* RHE in 0.2 M PBS electrolyte. The CV curve shows a cathodic peak at 0.56 V, which indicates the reduction of SnO_2 to SnO (Fig. S7). On the other hand, the two anodic peaks stem from Sn oxidization to SnO (at 0.09 V) and its further oxidization into SnO_2 (at 0.42 V) [47-48]. The reproducible CV curves are obtained after 20 sweeping cycles, indicating the formation of a stable surface composition. Because the intensity of characteristic peak is proportional to the corresponding percentage of tin species [49-50], the percentage of Sn species can be estimated by integrating the redox peak, as depicted in Fig. S7b. The ratio of SnO_2:SnO:Sn is about 91:2:7. Therefore, the majority of Sn species on the surface is SnO_2, which is consistent with the XPS analysis (Fig. S5).

3.2 HER Performance of Nanoporous Catalysts

To evaluate the HER electrocatalytic performance of nanoporous electrocatalysts, self-supported NP Au-SnO_x and NPG after dealloying can be directly used as electrodes for electrochemical measurements in a N_2-purged 0.2 M PBS electrolyte (pH = 7.0). All electrochemical measurements were performed on a CHI 760E electrochemical workstation with a typical three-electrode cell (Fig. S8). Fig. 4(a) shows the HER polarization curves of normalized current densities *vs.* applied potential (*i*R corrected) plot for a representative NP Au-SnO_x electrocatalyst, in combination with that of the NPG and commercially

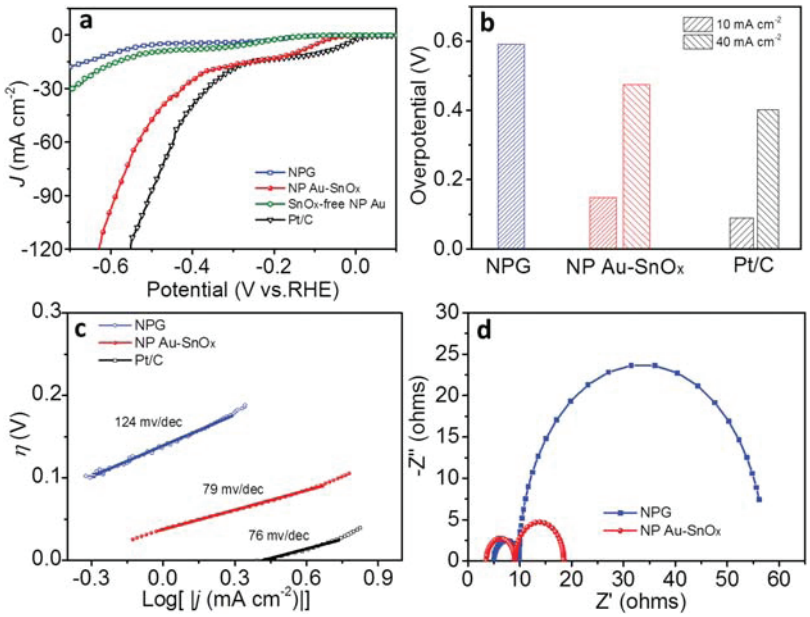

Figure 4: HER electrocatalytic activity of nanoporous catalysts in 0.2 M PBS aqueous electrolyte. a) Polarization curves of the NPG, NP Au-SnO_x and Pt/C electro catalysts. The scan rates are 5 mV s^{-1}. b) Overpotentials of the NPG, NP Au-SnO_x and Pt/C electrocatalysts at 10 and 40 mA cm^{-2}. c) The corresponding Tafel plots for the NPG, NP Au-SnO_x and Pt/C electrocatalysts. d) Nyquist plots of the NPG and NP Au-SnO_x in 0.2 M PBS aqueous electrolyte at room temperature

available Pt/C catalysts (20 wt%) for comparison. Different from the behavior of the NPG, the NP Au-SnO_x exhibits remarkably enhanced HER activity with very low onset overpotential (η_0) of 38 mV *vs.* reversible hydrogen electrode (RHE), and the current density rapidly increases to 10 mA cm^{-2} at the overpotential (η_{10}) of 148 mV without electrode rotation or stirring the electrolyte. Both η_0 and η_{10} values are lower than these of the NPG (η_0 = 110 mV and η_{10} = 591 mV). These results demonstrate that introducing SnO_x in the NPG can enhance HER activity effectively. Furthermore, the overpotential for the NP Au-SnO_x at the current density of 40 mA cm^{-2} (475 mV) is only 73 mV higher than Pt/C (402 mV, Fig. 4(b)), indicating that the NP Au-SnO_x possess comparable performance with Pt/C at high overpotential.

To explore the intrinsic mechanism of the high activity in the NP Au-SnO_x and evaluate the contribution of SnO_x on the surface, a SnO_x-free nanoporous Au with identical porous structure was synthesized by performing one additional dealloying in 6 M HCl solution to remove the SnO_x from the NP Au-SnO_x surface. The CV measurement confirms that there is no redox peak corresponding to tin oxide after additional dealloying, indicating the successful removal of SnO_x from the surface. As expected, the HER activity of the SnO_x-free NP Au decreases significantly relative to the NP Au-SnO_x, behaving the similar performance of the NPG. Based on the electrocatalysis results for both NPG and SnO_x-free NP Au, it can be concluded that the exceptional HER activity observed in the NP Au-SnO_x is due to the existence of gradient SnO_x in nanoporous ligaments.

Tafel analysis is performed with an attempt to gain insights into the HER kinetics. The linear portions of the Tafel plots were fitted to the Tafel equation ($\eta = a + b\log|j|$) and yielded the slope (b). As shown in Fig. 4(c), the NP Au-SnO_x exhibits a Tafel slope of 79 mV/dec (η = 36-90 mV), and is very close to the value of Pt/C (76 mV/dec). However, the NPG displays a Tafel slope of 124 mV/dec, implying that the

rate-limiting step is the Volmer step (120 mV/dec). A smaller Tafel slope for the NP Au-SnO_x indicates better catalytic performance relative to the NPG. The geometric exchange current density (J_0) of the NP Au-SnO_x electrode that is calculated from the Tafel plot data is 0.34 mA cm^{-2}, which is over 4 times higher than that of the NPG (0.08 mA cm^{-2}). The large exchange current density of the NP Au-SnO_x indicates higher intrinsic electrocatalytic activity than the NPG for HER. These electrocatalytic results are summarized in Tab. S1, and additional data from recent investigations on some representative HER electro catlysts in neutral medium are also included for comparison.

To quantitatively demonstrate the enhanced HER activities of the NP Au-SnO_x electrodes, the specific activities are calculated by dividing the current at the overpotential of 200 mV by the electrochemical active surface areas (ECSA) that are evaluated by the double-layer capacitance (C_{dl}) measurements. According to the CV curve in a potential window of −0.2 V to −0.4 V (*vs*. SCE) at various scan rates, the C_{dl} values are estimated by the linear slope in the plot of capacitive current density at −0.3 V against scan rate (Fig. S9). The ECSAs are further calculated using a constant factor of ≈17 μF/cm^2 corresponding to Au planar surface [51]. As shown in Fig. S9d, the specific activity of the NP Au-SnO_x at the overpotential of 200 mV reaches 3.3 μA cm^{-2}, almost three times as high as that of the NPG (1.2 μA cm^{-2}). This evidence demonstrates that the high activity of the NP Au-SnO_x derived from the intrinsic highly activity per site, which may stem from the high activity of metal/oxide interfaces and good conductivity of Au skeleton.

Notably, the HER polarization curves for three catalysts in neutral electrolyte can be clearly divided into two stages: the first one is a slowly increasing stage of current density with applied potential from the onset potential to a transition potential E_t (Pt/C: −0.3 V *vs.* RHE, NP Au-SnO_x: −0.4 V *vs.* RHE, NPG: −0.5 V *vs.* RHE); the second stage corresponds to a sharp increase of current density beyond the transition potential. In neutral conditions, the HER on a transition metal surface is expected to proceed in either Volmer-Heyrovsky or Volmer-Tafel mechanisms [52]:

Volmer step : $H_3O^+ + e^- + * \leftrightarrow H^* + H_2O$

Heyrovsky step : $H_3O^+ + e^- + H^* \leftrightarrow H_2 + H_2O$

Tafel step : $H^* + H^* \leftrightarrow H_2$

where * represents the hydrogen adsorption sites. The proton can be acquired from $H_2PO_4^-$, HPO_4^{2-} and H_2O in PBS solution. In fact, $H_2PO_4^-$ and HPO_4^{2-} are actually better hydrogen donors although the concentration is far below than that of H_2O in electrolyte. Therefore, a potential mechanism is that $H_2PO_4^-$ and HPO_4^{2-} offers proton for HER at the first stage. But it cannot keep sustainable as the proton is depleted quickly at high overpotential because of the limited migration of $H_2PO_4^-$ and HPO_4^{2-} in the nanoporous structure. So the local pH increases and turns to be alkaline near the catalyst surface [53-54], and H_2O offers proton for the HER at the second stage in the Volmer process: $H_2O+e^- + * \leftrightarrow H^* + OH^-$. The catalyst needs to break the H-O-H bond before adsorbing H*, which is more difficult to pursue than the reduction of H_3O^+ [14, 55-56]. Therefore, it requires high overpotential in the second stage.

It is reported recently that metal/oxide heterostructures, such as Ni/NiO heterostructure [45] and Co/Co_3O_4 core-shells [46, 57], are able to promote the water dissociation step in alkaline media because of strong interactions between the adsorbed H_2O species and oxide surfaces. The OH^- could preferentially attach to metal oxide at the heterojunctions for the strong electrostatic attraction between metal ions to OH^-; meanwhile, H^+ prefers to adsorb at the neighboring site of metal. The strong interfacial interaction between metal and oxide, particularly the interface confinement effect in supported nanostructures, has been suggested to provide and stabilize highly active sites for molecular activation [30]. On the other hand, density functional theory (DFT) calculations suggested that the metal/oxide heterostructure possesses a lower water dissociation free energy and a more optimal HBE than the counterparts [58-59].

Weng et al. reported that the metal/oxide interfaces between Ni and CeO_2 not only facilitates the dissociation of water molecules but also modifies the HBE to the same level of Pt [60]. Therefore, there is a plausible scenario that SnO_x oxide in NP Au-SnO_x surface would promote the HER catalysis in a similar manner, which could make the significant enhancement of HER activity. As schematically depicted in Fig. 5, we propose that the mechanisms involved in the HER activity with and without SnO_x. It is clear that water adsorption at the SnO_x/Au heterojunction sites is strengthened due to concerted interaction of O atoms with SnO_x domains and H atoms with Au (Fig. 5(b)) [34]. However, without SnO_x on the surface, only H atoms can adsorb on the metal surface. Water adsorption is then followed by water dissociation and hydrogen adsorption (H_{ad}) on the nearby vacant Au sites. Finally, two H_{ad} atoms on the metal surface recombine to form H_2 (H_2 desorption step)and OH^- desorbs from the SnO_x domains, followed by adsorption of another water molecule on the same site [61].

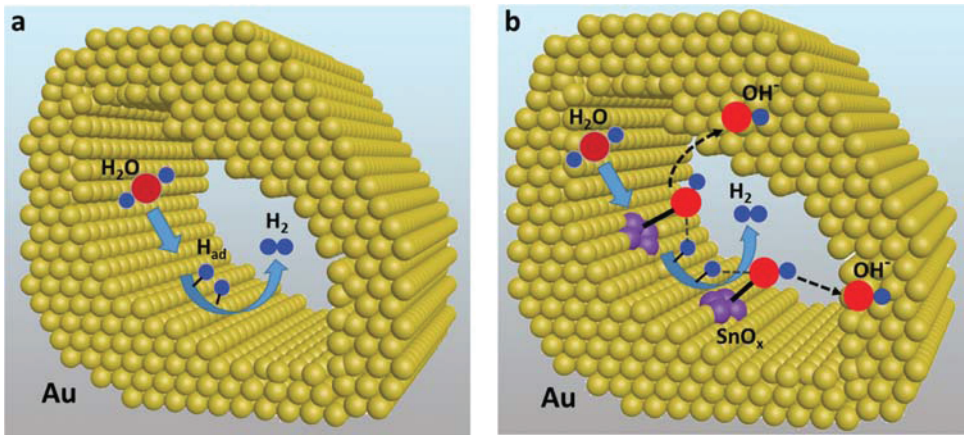

Figure 5: Schematic representation of water dissociation to hydrogen production in neutral media. a) Only H atoms adsorbs on the Au surface for NPG catalyst. b) Water adsorption is strengthened by concerted interaction of O atoms with SnO_x domians for NP Au-SnO_x catalyst

The key issue for the HER in neutral media is the high Ohmic loss and the interfacial charge-transfer resistance between electrode and electrolyte. In order to clarify the distinct electrochemical behaviors of the NP Au-SnO_x and NPG electrodes, their electrochemical impedance spectroscopy (EIS) analysis is further conducted in a frequency range from 1000 kHz to 10 mHz under hydrogen evolution voltage of −0.15 V *vs*. RHE (corresponds to the potential at 10 mA cm^{-2}) [14], as shown in Fig. 4(d). The Nyquist plots of the NPG and NP Au-SnO_x electrodes display two semicircles in high- and low-frequency ranges, which indicate the presence of two time constants related to HER kinetics. In order to fit the impedance spectra, a serial model containing two constant phase elements was used to analyze the EIS spectra (inset of Fig. S10), wherein R_s is the intrinsic electrode and electrolyte resistance, R_p is the resistance of nanopores, R_{ct} is the charge transfer resistance; C_p is the constant phase elements corresponding to the capacitance of nanopores, and C_d is the constant phase elements corresponding to the double-layer capacitance [62-63]. These parameters of R_s, R_p and R_{ct} are summarized in Fig. S10. Measurement errors in fitting impedance data were ≤6.8% for NP Au-SnOx, and ≤7.4% for NPG, respectively. Owing to their similar conductive Au skeleton and pore size (Fig. S1), both the NPG and NP Au-SnO_x electrodes almost have the same R_s and R_p values. In contrast, the NP Au-SnO_x possesses a low R_{ct} value of 5.5 Ω, much smaller than that of the NPG (47.8 Ω). The lower R_{ct} value indicates a faster hydrogen reaction rate and enhanced HER activity [14, 46, 62]. Therefore, the enhanced HER performance of NP Au-SnOx was likely due to the low R_{ct} on the electrode surface caused by the gradient SnO_x oxide. Meanwhile, the

self-supported nanoporous structure facilitates the mass transportation and the highly conductive metallic skeleton grants the fast electron transfer process.

3.3 The Stability of Nanoporous Catalysts

To evaluate the catalytic durability, 10 hours electrolysis is performed at −0.4 V *vs.* RHE without *i*R correction in N_2-saturated 0.2 M PBS solution, as shown in Fig. 6(a). The current density for both the NP Au-SnO_x and NPG can maintain stable within 10 hours without abrupt decay. Furthermore, the HER polarization curve of the NP Au-SnO_x after 10 hours is similar to the original one prior to long-term stability test (Fig. 6(b)).The current density only shows a slight decrease in the first stage (before −0.4 V) and exhibits a weak enhancement in the second stage (after −0.4 V), suggesting its high durability. In order to investigate the stability of SnO_x in long-term electrolysis, the NP Au-SnO_x after catalysis evaluation was further detected by the XPS (Fig. 6(c)). The spectrum of Sn 3d shows almost the same after 10 hours electrolysis, indicating the identical chemical states of the oxide in surface as before. This may result from the gradient oxide structure on the ligament surface, that possesses higher stability under electrochemical catalytic condition compared to the nanoparticle or core-shell structure [64-65]. Another possibility is that neutral electrolyte is less corrosive and has negligible effect on electrode material. So metal/oxide interfaces in the ligament can remain stable during long-term electrochemical test. The HER polarization curves are also tested in 0.5 M H_2SO_4 and 0.1 M KOH, and the NP Au-SnO_x also represents higher activity in comparison with the NPG in acidic and alkaline electrolytes (Fig. S11). However, the catalytic activity of the NP Au-SnO_x in alkaline environment decreases quickly after 200 continuous cycling linear sweep voltammetry (LSV), indicating the degeneration of catalytic activities (Fig. S12).

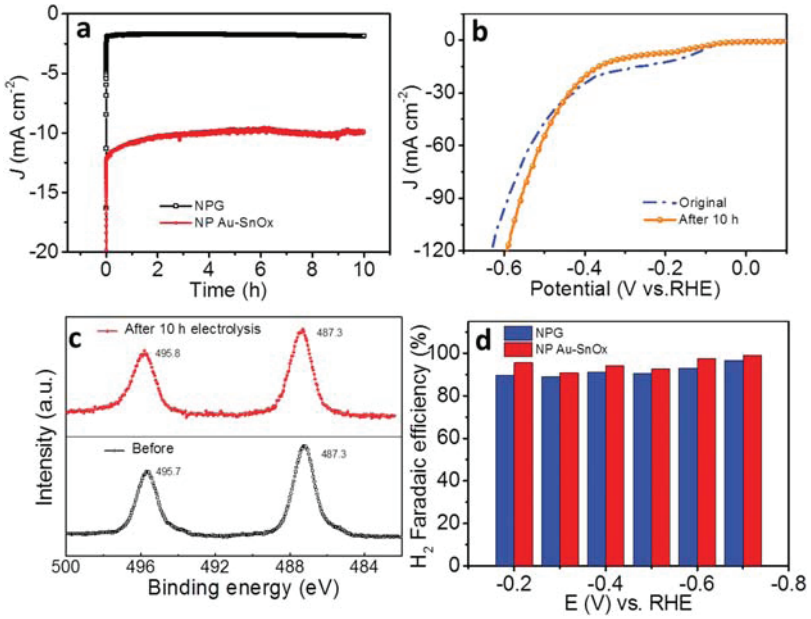

Figure 6: Durability tests for the NPG and NP Au-SnO_x. a) Current density *vs.* time (*I–t*) curves of the NPG and NP Au-SnO_x at −0.4 V *vs.* RHE in N_2-saturated 0.2 M PBS solution. b) Polarization curves of the NP Au-SnO_x catalysts before and after 10 h electrolysis. c) Sn 3d XPS spectra of the NP Au-SnO_x before and after 10 h electrolysis. d) Faradaic efficiency of H_2 at various potentials for the NPG and NP Au-SnO_x in 0.2 M PBS electrolyte

To further verify whether metal oxides were reduced during HER process, gas products were analyzed by gas chromatography (GC) to determine the corresponding Faradaic efficiency (FE). Electrolysis was performed in a gas-tight electrochemical cell with two compartments separated by a piece of anion exchange membrane. Gas-phase product from one identical sample was automatically sampled in 15 min for quantitative analysis from −0.2 V to −0.7 V *vs*. RHE. Fig. 6(d) shows the H_2 FE at various potentials in N_2-saturated 0.2 M PBS. For both the NPG and NP Au-SnO_x catalysts, the FE of hydrogen reaches above 90%. If metal oxides were reduced to metal and make the significant contribution to the current, the FE of the NP Au-SnO_x would be less than that of the NPG. However, there is no difference between the FEs for the NP Au-SnO_x and the NPG within the range of −0.2 V to −0.7 V *vs*. RHE. Therefore, it can be concluded that metal oxides with gradient structure in the ligament would not be reduced during HER process, indicating its remarkable stability.

4 Conclusions

In summary, the addition of SnO_x into nanoporous gold is identified to be highly active and durable for the HER under neutral media. The NP Au-SnO_x features a low onset overpotential of 38 mV and a small Tafel slope of 79 mV dec^{-1}, and displays the current density of 10 mA cm^{-2} at an overpotential as low as 148 mV in neutral electrolyte, which is comparable to that of the Pt/C catalyst. Relative to the NPG, the improved catalytic performance of NP Au-SnO_x results from the gradient SnO_x structure and metal/oxide interfaces. Moreover, gradient oxide in the ligament provides structural stability for long-term reaction. The idea and concept delivered in this work can be extended toward nanoporous transition metals with low cost, such as Ni and Mo alloys. The insights in this study may serve as a principle to design high performance HER catalysts for water splitting in neutral media in the future.

Acknowledgement: We acknowledge financial support from the National Natural Science Foundation of China (51771078, 91545131 and 51371084) and China Postdoctoral Science Foundation (No. 2017M612455). XPS characterizations were carried out in Analytical and Testing Center in HUST. Microstructural characterizations (SEM & TEM) were carried out in State Key Laboratory of MPDMT.

Conflicts of Interest: The authors declare that they have no conflicts of interest to report regarding the present study.

References

1. Zhao, G., Rui, K., Dou, S. X., Sun, W. (2018). Heterostructures for electrochemical hydrogen evolution reaction: a review. *Advanced Functional Materials, 28(43),* 1803291. DOI 10.1002/adfm.201803291.
2. Yao, Z., Yan, J., Mietek, J., Zhang, Q. S. (2015). Advancing the electrochemistry of the hydrogen-evolution reaction through combining experiment and theory. *Angewandte Chemie International Edition, 54(1),* 52–65.
3. Wang, H., Gao, L. (2018). Recent developments in electrochemical hydrogen evolution reaction. *Current Opinion in Electrochemistry, 7,* 7–14. DOI 10.1016/j.coelec.2017.10.010.
4. Lewis, N. S., Nocera, D. G. (2006). Powering the planet: chemical challenges in solar energy utilization. *Proceedings of the National Academy of Sciences of the United States of America, 103(43),* 15729–15735.
5. Zou, X., Zhang, Y. (2015). Noble metal-free hydrogen evolution catalysts for water splitting. *Chemical Society Reviews, 44(15),* 5148–5180. DOI 10.1039/C4CS00448E.
6. Laursen, A. B., Varela, A. S., Dionigi, F., Fanchiu, H., Miller, C. et al. (2012). Electrochemical hydrogen evolution: Sabatier's principle and the volcano plot. *Journal of Chemical Education, 89(12),* 1595–1599.
7. Sheng, W., Myint, M., Chen, J. G., Yan, Y. (2013). Correlating the hydrogen evolution reaction activity in alkaline electrolytes with the hydrogen binding energy on monometallic surfaces. *Energy & Environmental Science, 6(5),* 1509–1512. DOI 10.1039/c3ee00045a.

8. Li, Y., Zhang, H., Xu, T., Lu, Z., Wu, X. et al. (2015). Under-water superaerophobic pine-shaped Pt nanoarray electrode for ultrahigh-performance hydrogen evolution. *Advanced Functional Materials, 25(11),* 1737–1744. DOI 10.1002/adfm.201404250.
9. Greeley, J., Jaramillo, T. F., Bonde, J., Chorkendorff, I. B., Nørskov, J. K. (2006). Computational high-throughput screening of electrocatalytic materials for hydrogen evolution. *Nature Materials, 5(11),* 909–913. DOI 10.1038/nmat1752.
10. Zhang, J., Wang, T., Liu, P., Liao, Z., Liu, S. et al. (2017). Efficient hydrogen production on MoNi4 electrocatalysts with fast water dissociation kinetics. *Nature Communications, 8,* 15437.
11. Tan, Y., Wang, H., Liu, P., Cheng, C., Zhu, F. et al. (2016). 3D nanoporous metal phosphides toward high-efficiency electrochemical hydrogen production. *Advanced Materials, 28(15),* 2951–2955.
12. Tan, Y. W., Wang, H., Liu, P., Shen, Y. H., Cheng, C. et al. (2016). Versatile nanoporous bimetallic phosphides towards electrochemical water splitting. *Energy & Environmental Science, 9(7),* 2257–2261. DOI 10.1039/C6EE01109H.
13. Gao, J. J., Luo, P., Qiu, H. J., Wang, Y. (2017). Nanoporous FeP nanorods grown on Ti plate as an enhanced binder-free hydrogen evolution cathode. *Nanotechnology, 28(10),* 105705.
14. Jing, W., Fan, X., Haiyan, J., Yiqing, C., Yong, W. (2017). Non-noble metal-based carbon composites in hydrogen evolution reaction: fundamentals to applications. *Advanced Materials, 29(14),* 1605838.
15. Zou, X. X., Huang, X. X., Goswami, A., Silva, R., Sathe, B. R. et al. (2014). Cobalt-embedded nitrogen-rich carbon nanotubes efficiently catalyze hydrogen evolution reaction at all pH values. *Angewandte Chemie International Edition, 53(17),* 4372–4376. DOI 10.1002/anie.201311111.
16. Zhang, P., Wang, M., Chen, H., Liang, Y., Sun, J. et al. (2016). A Cu-based nanoparticulate film as super-active and robust catalyst surpasses Pt for electrochemical H_2 production from neutral and weak acidic aqueous solutions. *Advanced Energy Materials, 6(8),* 1502319. DOI 10.1002/aenm.201502319.
17. Wen, L., Sun, Y., Zhang, T., Bai, Y., Li, X. et al. (2018). $MnMoO_4$ nanosheet array: an efficient electrocatalyst for hydrogen evolution reaction with enhanced activity over a wide pH range. *Nanotechnology, 29(33),* 335403.
18. Merki, D., Vrubel, H., Rovelli, L., Fierro, S., Hu, X. L. (2012). Fe, Co, and Ni ions promote the catalytic activity of amorphous molybdenum sulfide films for hydrogen evolution. *Chemical Science, 3(8),* 2515–2525.
19. Callejas, J. F., McEnaney, J. M., Read, C. G., Crompton, J. C., Biacchi, A. J. et al. (2014). Electrocatalytic and photocatalytic hydrogen production from acidic and neutral-pH aqueous solutions using iron phosphide nanoparticles. *ACS Nano, 8(11),* 11101–11107.
20. Tian, J. Q., Liu, Q., Liang, Y. H., Xing, Z. C., Asiri, A. M. et al. (2014). FeP nanoparticles film grown on carbon cloth: An ultrahighly active 3D hydrogen evolution cathode in both acidic and neutral solutions. *ACS Applied Materials & Interfaces, 6(23),* 20579–20584. DOI 10.1021/am5064684.
21. Pu, Z. H., Liu, Q., Jiang, P., Asiri, A. M., Obaid, A. Y. et al. (2014). CoP nanosheet arrays supported on a Ti plate: an efficient cathode for electrochemical hydrogen evolution. *Chemistry of Materials, 26(15),* 4326–4329.
22. Gu, S., Du, H. F., Asiri, A. M., Sun, X. P., Li, C. M. (2014). Three-dimensional interconnected network of nanoporous CoP nanowires as an efficient hydrogen evolution cathode. *Physical Chemistry Chemical Physics, 16(32),* 16909–16913.
23. Sun, Y. J., Liu, C., Grauer, D. C., Yano, J. K., Long, J. R. et al. (2013). Electrodeposited cobalt-sulfide catalyst for electrochemical and photoelectrochemical hydrogen generation from water. *Journal of the American Chemical Society, 135(47),* 17699–17702. DOI 10.1021/ja4094764.
24. Yang, Y., Lin, Z. Y., Gao, S. Q., Su, J. W., Lun, Z. Y. et al. (2017). Tuning electronic structures of nonprecious ternary alloys encapsulated in graphene layers for optimizing overall water splitting activity. *ACS Catalysis, 7(1),* 469–479.
25. Xu, X., Liang, H., Ming, F., Qi, Z., Xie, Y. et al. (2017). Prussian blue analogues derived penroseite $(Ni,Co)Se_2$ nanocages anchored on 3D graphene aerogel for efficient water splitting. *ACS Catalysis, 7(9),* 6394–6399.
26. Shi, J. L., Hu, J. M. (2015). Molybdenum sulfide nanosheet arrays supported on Ti plate: an efficient hydrogen-evolving cathode over the whole pH range. *Electrochimica Acta, 168,* 256–260. DOI 10.1016/j.electacta.2015.03.157.

27. Liu, B. R., Zhang, L., Xiong, W. L., Ma, M. M. (2016). Cobalt-nanocrystal-assembled hollow nanoparticles for electrocatalytic hydrogen generation from neutral-pH water. *Angewandte Chemie International Edition, 55(23),* 6725–6729. DOI 10.1002/anie.201601367.
28. Feng, L. L., Fan, M. H., Wu, Y. Y., Liu, Y. P., Li, G. D. et al. (2016). Metallic Co_9S_8 nanosheets grown on carbon cloth as efficient binder-free electrocatalysts for the hydrogen evolution reaction in neutral media. *Journal of Materials Chemistry A, 4(18),* 6860–6867. DOI 10.1039/C5TA08611F.
29. Ge, X., Chen, L., Zhang, L., Wen, Y., Hirata, A. et al. (2014). Nanoporous metal enhanced catalytic activities of amorphous molybdenum sulfide for high-efficiency hydrogen production. *Advanced Materials, 26(19),* 3100–3104.
30. Yang, F., Deng, D., Pan, X., Fu, Q., Bao, X. (2015). Understanding nano effects in catalysis. *National Science Review, 2(2),* 183–201. DOI 10.1093/nsr/nwv024.
31. Zhang, P., Li, L., Nordlund, D., Chen, H., Fan, L. et al. (2018). Dendritic core-shell nickel-iron-copper metal/metal oxide electrode for efficient electrocatalytic water oxidation. *Nature Communications, 9,* 381.
32. Cheng, P., Yuan, C., Zhou, Q., Hu, X., Li, J. et al. (2019). Core-shell MoS2@CoO electrocatalyst for water splitting in neural and alkaline solutions. *Journal of Physical Chemistry C, 123(10),* 5833–5839.
33. Zhai, S., Zhao, H. (2019). Silica-coated metallic nanoparticle-based hierarchical super-hydrophobic surfaces fabricated by spin-coating and inverse nanotransfer printing. *Applied Physics Letters, 114(23),* 233702.
34. Xu, H., Zhang, R. Q., Ng, A. M. C., Djurisic, A. B., Chan, H. T. et al. (2011). Splitting water on metal oxide surfaces. *Journal of Physical Chemistry C, 115(40),* 19710–19715.
35. Lang, X., Hirata, A., Fujita, T., Chen, M. (2011). Nanoporous metal/oxide hybrid electrodes for electrochemical supercapacitors. *Nature Nanotechnology, 6(4),* 232–236.
36. Zhang, C., Qian, L., Zhang, K., Yuan, S., Xiao, J. et al. (2015). Hierarchical porous Ni/NiO core-shells with superior conductivity for electrochemical pseudo-capacitors and glucose sensors. *Journal of Materials Chemistry A, 3(19),* 10519–10525. DOI 10.1039/C5TA01071C.
37. Tan, Y., Liu, P., Chen, L., Cong, W., Ito, Y. et al. (2014). Monolayer MoS_2 films supported by 3D nanoporous metals for high-efficiency electrocatalytic hydrogen production. *Advanced Materials, 26(47),* 8023–8028.
38. Snyder, J., Asanithi, P., Dalton, A. B., Erlebacher, J. (2008). Stabilized nanoporous metals by dealloying ternary alloy precursors. *Advanced Materials, 20(24),* 4883–4886.
39. Weissmüller, J., Sieradzki, K. (2018). Dealloyed nanoporous materials with interface-controlled behavior. *MRS Bulletin, 43(1),* 14–19.
40. Qian, L. H., Yan, X. Q., Fujita, T., Inoue, A., Chen, M. W. (2007). Surface enhanced raman scattering of nanoporous gold: smaller pore sizes stronger enhancements. *Applied Physics Letters, 90(15),* 153120.
41. Ding, Y., Kim, Y. J., Erlebacher, J. (2004). Nanoporous gold leaf: "Ancient technology"/advanced material. *Advanced Materials, 16(21),* 1897–1900.
42. Baruch, M. F., Pander, J. E., White, J. L., Bocarsly, A. B. (2015). Mechanistic insights into the reduction of CO_2 on tin electrodes using in situ ATR-IR spectroscopy. *ACS Catalysis, 5(5),* 3148–3156.
43. Lee, S., Ocon, J. D., Son, Y. I., Lee, J. (2015). Alkaline CO_2 electrolysis toward selective and continuous $HCOO^-$ production over SnO_2 nanocatalysts. *Journal of Physical Chemistry C, 119(9),* 4884–4890.
44. Gao, D., Zhang, Y., Zhou, Z., Cai, F., Zhao, X. et al. (2017). Enhancing CO_2 electroreduction with the metal-oxide interface. *Journal of the American Chemical Society, 139(16),* 5652–5655. DOI 10.1021/jacs.7b00102.
45. Gong, M., Zhou, W., Tsai, M. C., Zhou, J. G., Guan, M. Y. et al. (2014). Nanoscale nickel oxide/nickel heterostructures for active hydrogen evolution electrocatalysis. *Nature Communications, 5,* 4695.
46. Yan, X., Tian, L., He, M., Chen, X. (2015). Three-dimensional crystalline/amorphous Co/Co_3O_4 core/shell nanosheets as efficient electrocatalysts for the hydrogen evolution reaction. *Nano Letters, 15(9),* 6015–6021.
47. Chen, Y., Kanan, M. W. (2012). Tin oxide dependence of the CO_2 reduction efficiency on tin electrodes and enhanced activity for tin/tin oxide thin-film catalysts. *Journal of the American Chemical Society, 134(4),* 1986–1989. DOI 10.1021/ja2108799.

48. Li, Q., Fu, J., Zhu, W., Chen, Z., Shen, B. et al. (2017). Tuning Sn-catalysis for electrochemical reduction of CO_2 to CO via the core/shell Cu/SnO_2 structure. *Journal of the American Chemical Society, 139(12),* 4290–4293. DOI 10.1021/jacs.7b00261.

49. Wang, Z., Liu, P., Han, J., Cheng, C., Ning, S. et al. (2017). Engineering the internal surfaces of three-dimensional nanoporous catalysts by surfactant-modified dealloying. *Nature Communications, 8,* 1066. DOI 10.1038/s41467-017-01085-3.

50. Barasa, G. O., Yu, T., Lu, X., Zhou, X., Wang, H. et al. (2019). Electrochemical training of nanoporous Cu-In catalysts for efficient CO_2-to-CO conversion and high durability. *Electrochimica Acta, 295,* 584–590. DOI 10.1016/j.electacta.2018.10.175.

51. Rouya, E., Cattarin, S., Reed, M. L., Kelly, R. G., Zangari, G. (2012). Electrochemical characterization of the surface area of nanoporous gold films. *Journal of the Electrochemical Society, 159(4),* K97–K102. DOI 10.1149/2.097204jes.

52. Skulason, E., Tripkovic, V., Bjorketun, M. E., Gudmundsdottir, S., Karlberg, G. et al. (2010). Modeling the electrochemical hydrogen oxidation and evolution reactions on the basis of density functional theory calculations. *Journal of Physical Chemistry C, 114(42),* 18182–18197.

53. Ma, M., Trzesniewski, B. J., Xie, J., Smith, W. A. (2016). Selective and efficient reduction of carbon dioxide to carbon monoxide on oxide-derived nanostructured silver electrocatalysts. *Angewandte Chemie International Edition, 55(33),* 9748–9752. DOI 10.1002/anie.201604654.

54. Gu, J., Heroguel, F., Luterbacher, J., Hu, X. (2018). Densely packed, ultra small SnO nanoparticles for enhanced activity and selectivity in electrochemical CO_2 reduction. *Angewandte Chemie International Edition, 57(11),* 2943–2947. DOI 10.1002/anie.201713003.

55. Morales-Guio, C. G., Stern, L. A., Hu, X. (2014). Nanostructured hydrotreating catalysts for electrochemical hydrogen evolution. *Chemical Society Reviews, 43(18),* 6555–6569. DOI 10.1039/C3CS60468C.

56. Durst, J., Siebel, A., Simon, C., Hasche, F., Herranz, J. et al. (2014). New insights into the electrochemical hydrogen oxidation and evolution reaction mechanism. *Energy & Environmental Science, 7(7),* 2255–2260. DOI 10.1039/C4EE00440J.

57. Zhang, C., Xiao, J., Lv, X., Qian, L., Yuan, S. et al. (2016). Hierarchically porous Co_3O_4/C nanowire arrays derived from a metal-organic framework for high performance supercapacitors and the oxygen evolution reaction. *Journal of Materials Chemistry A, 4(42),* 16516–16523. DOI 10.1039/C6TA06314D.

58. Zhang, R., Ren, X., Hao, S., Ge, R., Liu, Z. et al. (2018). Selective phosphidation: An effective strategy toward CoP/CeO_2 interface engineering for superior alkaline hydrogen evolution electrocatalysis. *Journal of Materials Chemistry A, 6(5),* 1985–1990. DOI 10.1039/C7TA10237B.

59. Wang, Z., Du, H., Liu, Z., Wang, H., Asiri, A. M. et al. (2018). Interface engineering of a CeO_2–Cu_3P nanoarray for efficient alkaline hydrogen evolution. *Nanoscale, 10(5),* 2213–2217.

60. Weng, Z., Liu, W., Yin, L. C., Fang, R., Li, M. et al. (2015). Metal/oxide interface nanostructures generated by surface segregation for electrocatalysis. *Nano Letters, 15(11),* 7704–7710.

61. Subbaraman, R., Tripkovic, D., Strmcnik, D., Chang, K. C., Uchimura, M. et al. (2011). Enhancing hydrogen evolution activity in water splitting by tailoring Li^+-$Ni(OH)_2$-Pt interfaces. *Science, 334(6060),* 1256–1260.

62. Sun, J. S., Wen, Z., Han, L. P., Chen, Z. W., Lang, X. Y. et al. (2018). Nonprecious intermetallic Al_7Cu_4Ni nanocrystals seamlessly integrated in freestanding bimodal nanoporous copper for efficient hydrogen evolution catalysis. *Advanced Functional Materials, 28(14),* 1706127.

63. Zhai, S., Zhao, H. (2016). Influence of concentration polarization on DNA translocation through a nanopore. *Physical Review E, 93(5),* 052409.

64. Wu, B., Yang, X., Jiang, X., Zhang, Y., Shu, H. et al. (2018). Synchronous tailoring surface structure and chemical composition of Li-rich-layered oxide for high-energy lithium-ion batteries. *Advanced Functional Materials, 28(37),* 1803392. DOI 10.1002/adfm.201803392.

65. Ma, J., Tong, X., Wang, J., Zhang, G., Lv, Y. et al. (2019). Rare-earth metal oxide hybridized PtFe nanocrystals synthesized via microfluidic process for enhanced electrochemical catalytic performance. *Electrochimica Acta, 299,* 80–88. DOI 10.1016/j.electacta.2018.12.132.

Appendix A

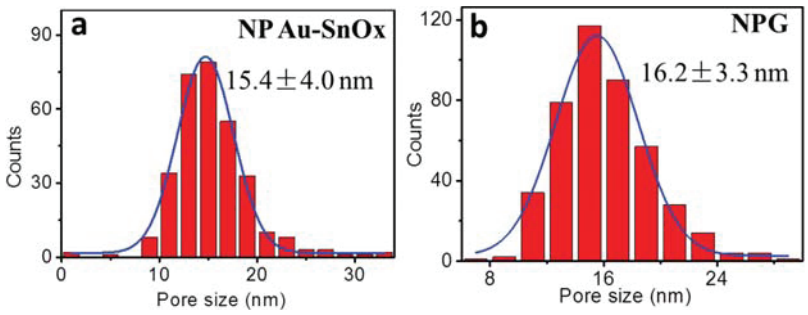

Figure S1: (a, b) Pore size distributions of the NP Au-SnO_x and NPG based on SEM images, respectively

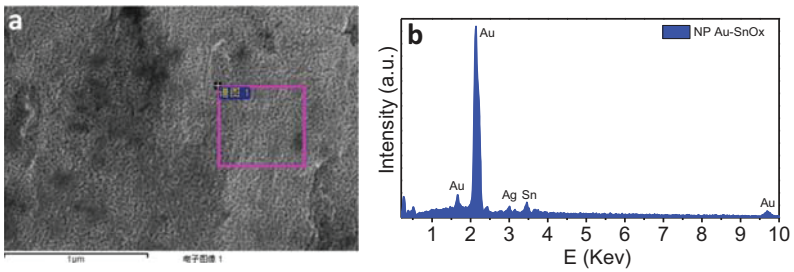

Element	wt.%	at.%	
Ag L	4.23	7.12	
Sn L	7.33	11.23	
Au M	88.45	81.65	
Total	100.00	100.00	

Figure S2: EDX analysis of the NP Au-SnO_x surface after dealloying

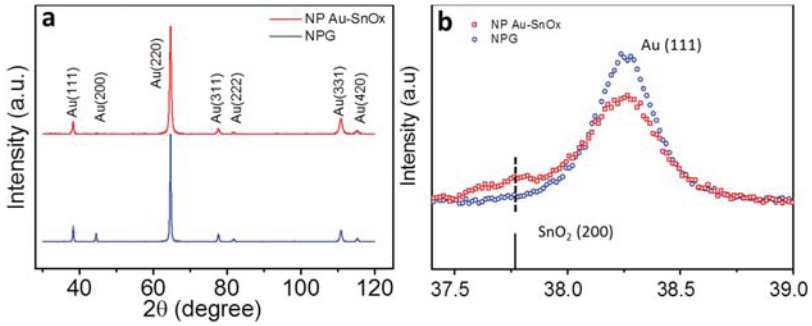

Figure S3: (a) XRD patterns of the NP Au-SnO_x and NPG. (b) The enlarged Au (111) peak region, the dotted line indicates a small shoulder peak corresponding to SnO_2 (200)

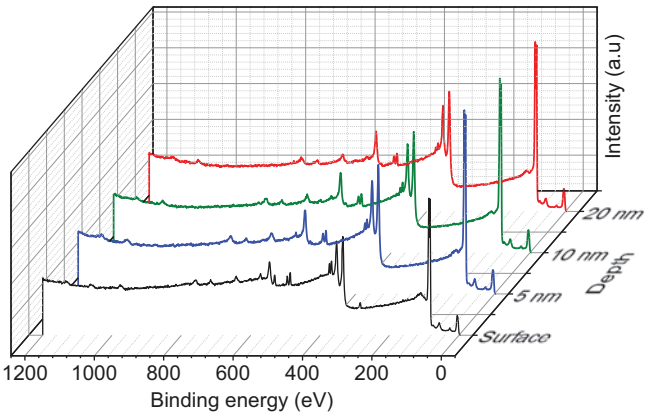

Figure S4: XPS survey spectra of the NP Au-SnO_x surface and at the depth of 5~20 nm

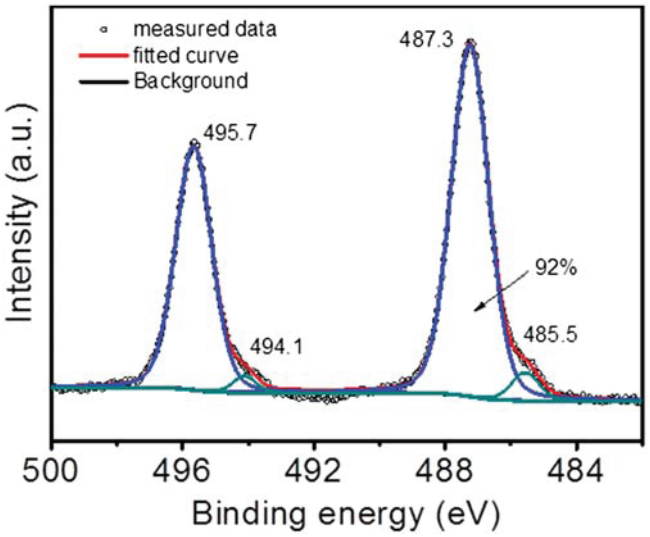

Figure S5: Sn 3d XPS spectrum of the NP Au-SnO_x surface. The spectrum is deconvoluted to calculate the percentage of SnO_2 by peak area

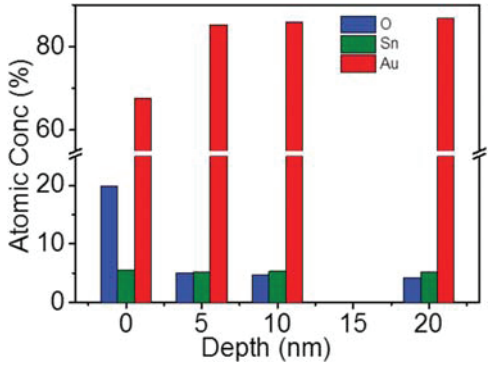

Figure S6: The atomic concentrations of Au, Sn and O atoms for the NP Au-SnO_x based on XPS quantification analysis

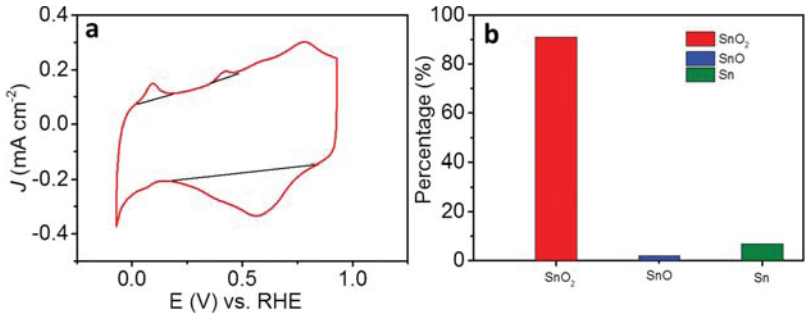

Figure S7: (a)CV curves of the NP Au-SnO_x in 0.2 M PBS. (b) The percentage of different Sn species in the NP Au-SnO_x surface

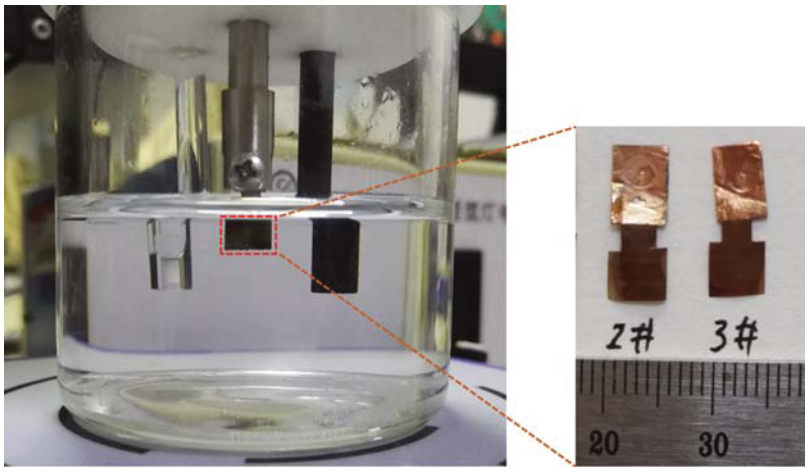

Figure S8: A typical three-electrode cell for HER studies, in which a graphite rod and an SCE reference electrode (saturated KCl) employed as the counter electrode and the reference electrode, respectively. Self-supported NP Au-SnO_x and NPG after dealloying were used as work electrodes directly

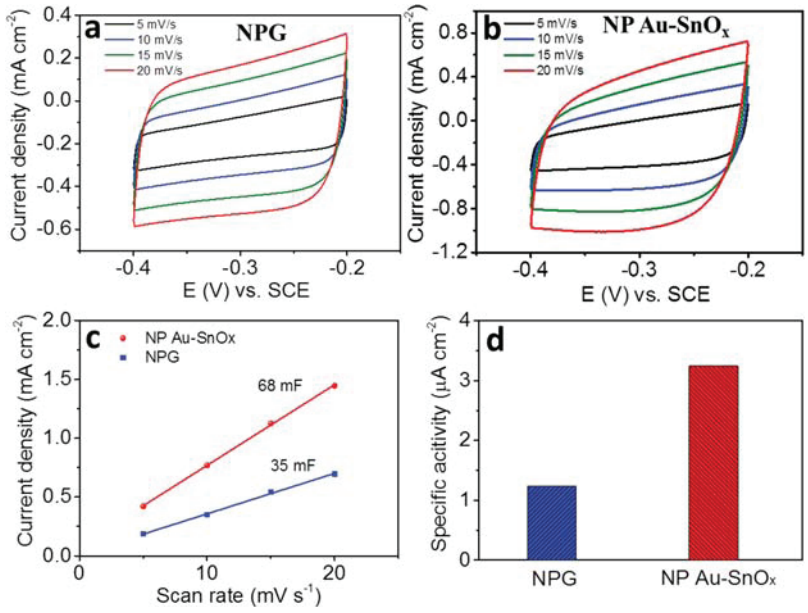

Figure S9: Electrochemical capacitance measurements for the estimation of electrochemical active surface areas (ECSAs) of the NPG and NP Au-SnO_x electrodes. (a, b) Cyclic voltammograms in the potential window for the NPG and NP Au-SnO_x electrodes at various scan rates, respectively. (c) The differences in current density at −0.3 V *vs.* SCE as a linear function of scan rate with the slope of double-layer capacitance, C_{dl}. (d) Comparison of specific activity for the NPG and NP Au-SnO_x electrodes. Here the specific activity is calculated by dividing the current density at the overpotential of 200 mV by the ECSAs that are evaluated by the double-layer capacitance (C_{dl}) measurements

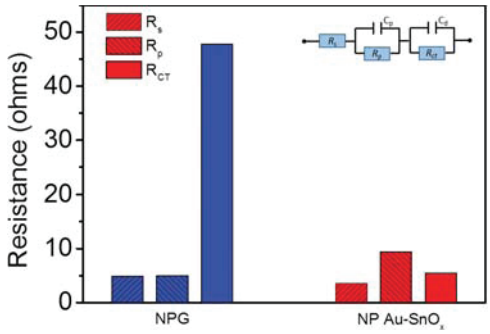

Figure S10: Comparison of R_s, R_p and R_{ct} for both the NPG and NP Au-SnO_x. Inset: The electrical equivalent circuit used for fitting EIS spectra, where R_s is the intrinsic electrode and electrolyte resistance, R_p is the resistance of nanopores, R_{ct} is the charge transfer resistance; C_p is the constant phase elements corresponding to the capacitance of nanopores, and C_d is the constant phase elements corresponding to the double-layer capacitance

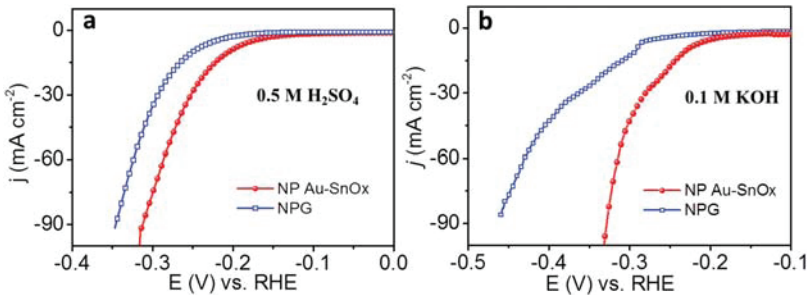

Figure S11: HER electrocatalytic activity of the NPG and NP Au-SnO_x catalysts in 0.5 M H_2SO_4 (a) and 0.1 M KOH (b) aqueous electrolyte, respectively. The scan rate is 5 mV s^{-1}

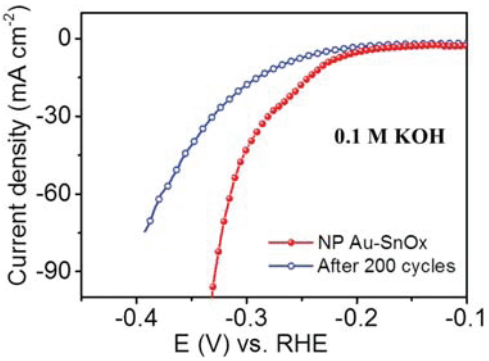

Figure S12: LSV curves for the NP Au-SnO_x catalyst before and after 200 continuous cycling LSV cycles in 0.1 M KOH

Table S1: Summary of HER performance for some representative electro catlysts in neutral media

Catalysts	Loading mass [mg cm^{-2}]	Electrolyte	pH	OP [mV]	η-j [η/mV]	TS [mV dec^{-1}]	J_0 [mA cm^{-2}]	Stability	Ref.
Cu-Cu_xO-Pt/GC	0.438	2 M PBS	7	10	45–20	44	1.601	100 h	[1]
H_2-CuCat/FTO	–	0.1 M KBi	9.2	450	440–1	320	–	12 h	[2]
H_2-CoCat/FTO	0.0589	0.5 M KBi	7	50	385–2	140	3.2×10^{-3}	–	[3]
Co-HNP/CC	1.0	1 M PBS	7	23	85–10	38	1.53	20 h, 1000 CV	[4]
FeP NPs/Ti	1.0	1 M PBS	7	–	102–10	–	–	16 h, 1000 CV	[5]
FeP NPs/CC	4.2	1 M PBS	7	50	125–10	70	–	22 h	[6]
FeP NAs/CC	1.5	1 M PBS	7	112	202–10	71	–	–	[7]
NP CoP Nws/Ti	0.8	1 M PBS	7	~80	178–10	125	–	1000 CV	[8]
CoP NAs/Ti	2.0	0.2 M PBS	7	100	149–10	58	–	1000 CV	[9]
Co-S/FTO	0.0796	1 M PBS	7	43	170–10	93	0.256	40 h	[10]
Hollow CoSnanoprosms/GC	0.283	1 M PBS	7	190	290–15	75	–	21 h	[11]
Co_9S_8/CC	–	1 M PBS	7	25	175–10	57.6	0.117	100 h	[12]
Ni_3S_2/Ni foam	1.5	1 M PBS	7	180	220–10	108		10 h	[13]
MoS2.7@NPG/ GC	–	0.2 M PBS	7	120	200–0.48	60	–	–	[14]
NPG film/GC	–	0.2 M PBS	7	–	200–0.12	132	–	–	[14]
Pt/C/GC	0.283	0.2 M PBS	7	~0	90–10 402–40	76	2.61	–	This work
NPG	**Self-supported**	0.2 M PBS	7	139	591–10	124	0.08	10 h	This work
NP Au-SnO_x	**Self-supported**	**0.2 M PBS**	**7**	**38**	**148–10 475–40**	**79**	**0.34**	**10 h**	**This work**
SnO_x free NP Au	**Self-supported**	**0.2 M PBS**	**7**	**145**	**506–10**	**118**	**0.06**	**–**	**This work**

Note: GC, glassy carbon electrode; FTO, fluorine-doped tin oxide electrode; CC, carbon cloth; OP represents onset overpotential; η-j represents the overpotential at a given current density j (mA cm^{-2}); TS represents the Tafel slope; J_0represents the exchange current density.

Ref. in Table S1

1. Zhang, P., Wang, M., Chen, H., Liang, Y., Sun, J., Sun, L. (2016). A Cu-based nanoparticulate film as super-active and robust catalyst surpasses Pt for electrochemical H_2 production from neutral and weak acidic aqueous solutions. *Advanced Energy Materials, 6(8)*, 1502319.
2. Liu, X., Zheng, H., Sun, Z., Han, A., Du, P. (2015). Earth-Abundant Copper-Based Bifunctional Electrocatalyst for Both Catalytic Hydrogen Production and Water Oxidation. *ACS Catalysis, 5(3)*, 1530-1538.
3. Cobo, S., Heidkamp, J., Jacques, P. A., Fize, J., Fourmond, V., Guetaz, L., Jousselme, B., Ivanova, V., Dau, H., Palacin, S., Fontecave, M., Artero, V. (2012). A Janus cobalt-based catalytic material for electro-splitting of water. *Nature Materials, 11(9)*, 802-807.
4. Liu, B. R., Zhang, L., Xiong, W. L., Ma, M. M. (2016). Cobalt-Nanocrystal-Assembled Hollow Nanoparticles for Electrocatalytic Hydrogen Generation from Neutral-pH Water. *Angewandte Chemie International Edition, 55(23)*, 6725-6729.
5. Callejas, J. F., McEnaney, J. M., Read, C. G., Crompton, J. C., Biacchi, A. J., Popczun, E. J., Gordon, T. R., Lewis, N. S., Schaak, R. E. (2014). Electrocatalytic and photocatalytic hydrogen production from acidic and neutral-pH aqueous solutions using iron phosphide nanoparticles. *ACS Nano, 8(11)*, 11101-11107.
6. Tian, J. Q., Liu, Q., Liang, Y. H., Xing, Z. C., Asiri, A. M., Sun, X. P. (2014). FeP nanoparticles film grown on carbon cloth: An ultrahighly active 3D hydrogen evolution cathode in both acidic and neutral solutions. *ACS Applied Materials & Interfaces, 6(23)*, 20579-20584.
7. Liang, Y., Liu, Q., Asiri, A. M., Sun, X., Luo, Y. (2014). Self-Supported FeP Nanorod Arrays: A Cost-Effective 3D Hydrogen Evolution Cathode with High Catalytic Activity. *ACS Catalysis, 4(11)*, 4065-4069
8. Gu, S., Du, H. F., Asiri, A. M., Sun, X. P., Li, C. M. (2014). Three-dimensional interconnected network of nanoporous CoP nanowires as an efficient hydrogen evolution cathode. *Physical Chemistry Chemical Physics, 16(32)*, 16909-16913.
9. Pu, Z. H., Liu, Q., Jiang, P., Asiri, A. M., Obaid, A. Y., Sun, X. P. (2014). CoP Nanosheet Arrays Supported on a Ti Plate: An Efficient Cathode for Electrochemical Hydrogen Evolution. *Chemistry of Materials, 26(15)*, 4326-4329.
10. Sun, Y. J., Liu, C., Grauer, D. C., Yano, J. K., Long, J. R., Yang, P. D., Chang, C. J. (2013). Electrodeposited Cobalt-Sulfide Catalyst for Electrochemical and Photoelectrochemical Hydrogen Generation from Water. *Journal of the American Chemical Society, 135(47)*, 17699-17702.
11. You, B., Jiang, N., Sheng, M., Sun, Y. (2015). Microwave vs. solvothermal synthesis of hollow cobalt sulfide nanoprisms for electrocatalytic hydrogen evolution and supercapacitors. *Chemical Communications, 51(20)*, 4252-4255.
12. Feng, L. L., Fan, M. H., Wu, Y. Y., Liu, Y. P., Li, G. D., Chen, H., Chen, W., Wang, D. J., Zou, X. X. (2016). Metallic Co_9S_8 nanosheets grown on carbon cloth as efficient binder-free electrocatalysts for the hydrogen evolution reaction in neutral media. *Journal of Materials Chemistry A, 4(18)*, 6860-6867.
13. Tang, C., Pu, Z., Liu, Q., Asiri, A. M., Luo, Y., Sun, X. (2015). Ni_3S_2 nanosheets array supported on Ni foam: A novel efficient three-dimensional hydrogen-evolving electrocatalyst in both neutral and basic solutions. *International Journal of Hydrogen Energy, 40(14)*, 4727-4732.
14. Ge, X., Chen, L., Zhang, L., Wen, Y., Hirata, A., Chen, M. (2014). Nanoporous metal enhanced catalytic activities of amorphous molybdenum sulfide for high-efficiency hydrogen production. *Advanced Materials, 26(19)*, 3100-3104.